



Robust Dual Equivariant Gradient Antibacterial Wound Dressing-Loaded Artificial Skin with Nano-chitin Particles Via an Electrospinning-Reactive Strategy

Lin Wang^{1,3} · Tengxiao Huang⁴ · Xiaowei Xu¹ · Nitong Bu¹ · Zhenzhen Wu¹ · Yunpeng Zhao⁴ · Ya-Qin Zhou² · Su Chen² · Yong Chen^{5,6} · Jie Pang¹

Received: 9 May 2024 / Accepted: 1 August 2024
© Donghua University, Shanghai, China 2024

Abstract

Excess biological fluids around skin wounds can lead to infections and impede the healing process. Researchers have extensively studied dressings with varying water contents for wound care. However, hydrophilic and hydrophobic-hydrophilic dressings often face challenges such as slow fluid transfer and excessive retention. This study introduces an innovative approach involving the use of superhydrophobic–hydrophobic–hydrophilic dual-gradient electrospun nanofibers to form a 3D biomimetic nanofiber scaffold (3D BNSF). The 3D BNSF is composed of hydrophobic polycaprolactone and thermoplastic polyurethane, along with antibacterial, superhydrophobic nano-chitin particles. In vitro and in vivo experiments have demonstrated that this scaffold exhibits excellent antibacterial properties and compatibility with cells, facilitating complete wound healing and regeneration. This study offers a new perspective on the targeted acceleration of wound healing, with the potential to become an alternative strategy for clinical applications.

Keywords Biomimetic nanofiber scaffolds · Dual equivariant gradient · Directional biofluid transport · Antibacterial · Superhydrophobicity · Wound dressings

1 Introduction

Wound exudate comprises fluid, cells, and cellular debris formed during inflammation and tissue damage in wound healing [1]. Its presence is vital in the early healing stages,

creating a moist environment for cell migration, providing nutrients and oxygen, eliminating waste, and containing antimicrobial elements to prevent infection [2–5]. However, excessive exudate can signal various issues, such as wound distortion, chronic inflammation, inadequate management,

✉ Su Chen
chensu@njtech.edu.cn

✉ Yong Chen
chenyong1982@njtech.edu.cn

✉ Jie Pang
pang3721941@163.com

¹ College of Food Science, Fujian Agriculture and Forestry University, Fuzhou 350002, China

² State Key Laboratory of Materials-Oriented Chemical Engineering and College of Chemical Engineering, Jiangsu Key Laboratory of Fine Chemicals and Functional Polymer Materials, Nanjing Tech University, Nanjing 210009, China

³ Key Laboratory of Colloid and Interface Chemistry of the Ministry of Education, School of Chemistry and Chemical Engineering, Shandong University, Jinan 250100, Shandong, China

⁴ Department of Orthopaedic Surgery, Qilu Hospital, Cheeloo College of Medicine, Shandong University, Jinan 250012, China

⁵ National Engineering Research Center for Biotechnology, College of Biotechnology and Pharmaceutical Engineering, Nanjing Tech University, Nanjing 210009, China

⁶ State Key Laboratory of Materials-Oriented Chemical Engineering, College of Biotechnology and Pharmaceutical Engineering, Nanjing Tech University, Nanjing 210009, China

and impaired angiogenesis [6–9]. Traditional dressings such as hydrogels [10], gauze, sponges, or common hydrophobic materials may exacerbate this issue due to their bidirectional liquid flow, limited breathability, and absorbency, leading to tearing, impaired blood flow, and the formation of tension blisters [11–13]. Hence, there is a clinical demand for wound dressings capable of unidirectional fluid transport and rapid absorption of large exudate volumes.

Deeper research into biological fluid management holds promise for reducing secondary infections and preventing overhydration reactions by efficiently transporting excess physiological tissue fluids [14]. Various attempts have been made, for example, although hydrogels have the ability to keep wounds moist, their mechanical strength [15, 16] and biomedical applications [17], which have always been of concern, have also made great progress. It can absorb exudates, but its ability to retain moisture may cause exudates to remain on the wound surface. The air permeability is usually limited, which also increases the risk of infection. In addition, nanofiber dressings made using 3D or 4D printing technology can provide customized structures to better adapt to the shape and size of specific wounds [18]. This customization capability enables dressings to provide personalized support and guidance while promoting tissue repair. Subsequently, biological fluids are manipulated by constructing a hydrophilic–hydrophobic gradient structure. This multilayer structure exhibits asymmetric surface wettability, unidirectional water transport ability, and a self-pumping effect, which can effectively eliminate biological fluids. Nanofibers with high surface areas and porous structures play a vital role in wound healing, providing an optimal platform for cell migration and proliferation and accelerating the wound-healing process [19]. Despite significant progress, the combination of nanofibers with superhydrophobic-hydrophobic-hydrophilic characteristics remains underexplored, and research on multi-wetting gradient nanofiber wound dressings is still in its early stages. Therefore, there is an urgent need for universally applicable methods that can guide the design of multifunctional nanofibers, artificial skin, and efficient biological fluid transport in both materials science and biomedicine [20].

Janus nanofibers, consisting of a hydrophobic fiber layer and a hydrophilic fiber layer, have been developed for wound healing dressings, offering controlled transport of wound fluids [21, 22]. Multilayered interwoven nanofiber networks possess remarkable flexibility, a large specific surface area, and a micro/nanoporous structure, making them appealing candidates for wound dressing fabrication [23, 24]. Recent advancements include various antibacterial methods or technologies, such as nanomaterial functionalization, the design of carriers for antibacterial agents, surface modification techniques, and the integration of bioactive substances [25, 26]. Techniques such as chemical modification or physical

adsorption are employed to enhance antibacterial activity by introducing antibacterial agents onto nanofiber surfaces [27, 28]. The integration of anti-inflammatory substances aids in healing, enhancing the therapeutic effectiveness and comprehensive treatment capability of nanofiber dressings [29, 30]. By embedding bioactive or antibacterial properties into the transfer layer, there is continuous directional water transport from the hydrophobic side to the superhydrophilic side, facilitating the transfer of bioactive or antibacterial components to the wound. Despite substantial efforts in creating surface energy gradients, achieving rapid response rates in water transport with multilayer nanofiber membranes has had limited success [31–33]. Most nanofibers are either hydrophilic, maintaining skin moisture for extended periods, or hydrophobic, lacking moisture transport capabilities. However, materials with asymmetric wetting properties exhibit robust directional water transport capabilities, enabling continuous sweat transport from one side to the other [34]. Designing wound dressings with directional fluid transport properties through manipulation of surface wetting gradients is crucial for preventing environmental infection in sensitive and fragile wounds.

This study ingeniously integrated three different wetting properties—superhydrophobic, hydrophobic, and hydrophilic—into a novel multilayer nanofiber wound dressing (3D BNSF) (Fig. 1). This dressing effectively provides an environment conducive to healing. The selected materials, including polycaprolactone (PCL), thermoplastic polyurethane (TPU), and nano-chitin fiber (CF), exhibit excellent biocompatibility and biodegradability. Notably, the modified CF not only has natural antibacterial properties but also enhances these properties with the addition of gallic acid (GA). By precisely controlling the diameter and alignment of the nanofibers, this study achieved optimized performance over traditional Janus nanofiber dressings, including precise control of the material composition, nanofiber arrangement, antibacterial properties, and mechanical strength. The design of this dressing addresses the complex requirements of wound healing, helping to accelerate the healing process and reduce complications. Furthermore, our exploration of integrated layered multiscale porous structures and dual-gradient fiber membrane engineering opens various pathways for rapid, directional biofluid transport and effective antibacterial action, thereby reducing the risk of infection during the wound healing process.

2 Materials and Experimental

Polycaprolactone (PCL), Gallic acid (GA), hexadecyltrimethoxysilane (HDTMS), γ -aminopropyl triethoxysilane (γ -AT), 1-ethyl-(3-dimethylaminopropyl) carbodiimide (EDC), N-hydroxysuccinimide (NHS), Citric acid (CA)

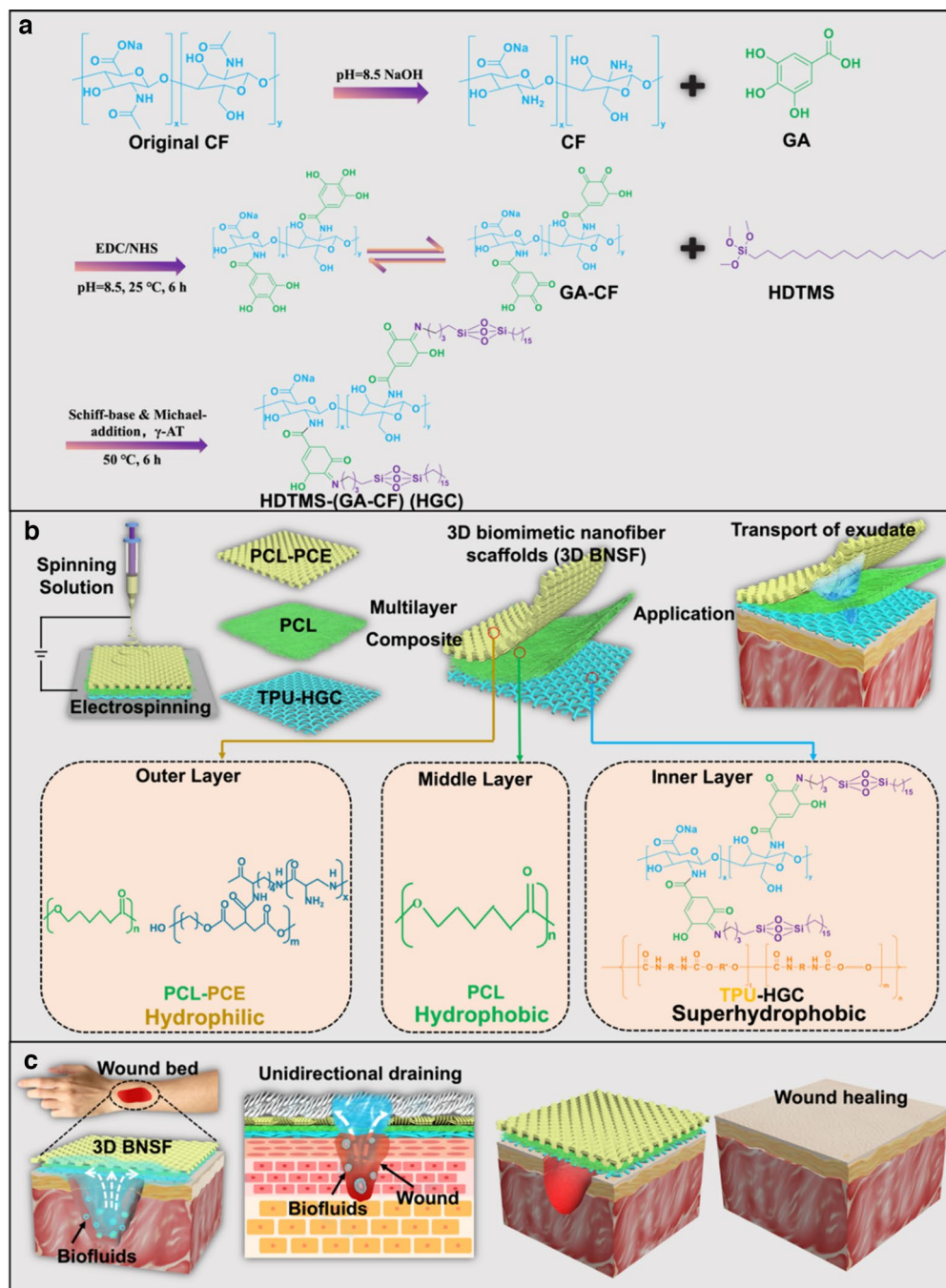


Fig. 1 Proposed design and application of 3D BNSF. **a** Schematic illustration of the fabrication process of HGC particles. **b** Schematic diagram of the superhydrophobic-hydrophobic-hydrophilic nanofiber scaffold prepared via the dual equivariant gradient method. The material exhibited absorption-transfer behavior: an inner TPU-HGC super-

hydrophobic layer (water absorption), an intermediate hydrophobic PCL layer, and an outer hydrophilic PCL-PCE layer (water transfer). **c** Schematic representation of biofluid transport and wound healing processes

(Shanghai Aladdin biochemical technology Co., Ltd). Trifluoroethanol (TFE), Dimethylformamide (DMF), thermoplastic polyurethane (TPU), dimethyl sulfoxide (DMSO), ethanol (Sinopharm Chemical Reagent Co.,

Ltd). ϵ -polylysine (EPL) and Nano chitin fiber (CF) (Beijing North Tianchen Technology Co., Ltd.). 1,8-octanediol (Nanjing Evening Chemical Glass Co., Ltd.). Calixanthin AM and propidium iodide (PI) (Nanjing Bono Biotech Co.,

Ltd.). Purple ink (Local supermarket). All other chemicals were used as received without further treatment.

2.1 Preparation of Superhydrophobic Particles

Preparation of liquid A: 2.0 g of nano chitin fiber (CF) was dissolved in 98 mL of ethanol and thoroughly stirred until completely dissolved. The solution was then sonicated to prepare the aqueous CF dispersion with a concentration of 2.0 wt%. 0.1 g of sodium hydroxide (NaOH) was dissolved in water to configure a concentration of 0.1 wt% NaOH solution to adjust the pH value of CF aqueous dispersion in the range of 8–9 [35].

Preparation of liquid B: Mix GA (0.2 g), EDC (0.232 g), and NHS (0.136 g) evenly and add to 10 mL of 30% ethanol aqueous solution. Stir in an ice bath for 1 h to obtain a GA mixture [36].

Solution A and solution B were rapidly mixed and stirred under ice bath conditions, and then stirred at room temperature for 24 h to finally obtain a GA-CF dispersion. HDTMS-(GA-CF) (HGC) superhydrophobic particles: Take 100 mL of GA-CF dispersion, add a certain amount of γ -AT (0.5 mL), stir for an hour, then weigh 2.0 mL of HDTMS, and dissolve it in the above solution at 50 °C solution, stir thoroughly, and then collect the precipitated HGC by centrifugation. The obtained HGC is sequentially redispersed in ethanol and centrifuged three times to remove free HDTMS. Further purification was performed by washing with deionized water and centrifuging several times. The supernatant was dialyzed for 1 week and freeze-dried to obtain superhydrophobic HGC particles.

2.2 Synthesis of PCE

The synthesis method of PCE was improved according to a literature procedure [37]: first, a certain amount of CA (4.0 g) and 1,8-octanediol (3.0 g) were weighed and mixed in a beaker, and then stirred at 160 °C until molten. The reaction was continued for 20 min to obtain the elastomeric prepolymer, which was then washed several times with a small amount of deionized water to remove the unreacted material and finally placed in an oven at room temperature for overnight drying for subsequent use (Fig. S1).

The same amounts of the dried elastomer prepolymer (2.0 g) and EPL (2.0 g) were separately weighed and dissolved in DMSO (12.0 g). Thereafter, EDC (1.0 g) and NHS (0.8 g) were added to the DMSO solution in turn, and the bionic elastomer PCE was obtained after stirring under heating conditions (60 °C) for 24 h. Finally, the PCE was stored in a refrigerator at 0–4 °C for subsequent use.

2.3 Preparation of 3D BNSF

First, three solutions (A, B, C) were prepared as electrostatic spinning solutions: (a). A quantitative amount of PCL and the bionic elastomer PCE was added to the TFE solution, and spinning solution A with 20 wt% concentration was obtained by stirring well, where the mass ratio of PCL to PCE was controlled to be 3:1. (b) A quantitative amount of PCL was added to TFE solution, followed by stirring well to obtain spinning solution B with 10 wt% concentration; (c) A certain amount of hydrophobic particles was added to DMF solution, followed by dispersion in an ultrasonic machine for 30 min. Subsequently, a certain amount of TPU was weighed and dissolved in the hydrophobic particle dispersion and then stirred well to obtain spinning solution C.

The 3D BNSF was prepared as follows: the material was fed through a pump at a constant feed rate (A: 0.6 mL/h) through a stainless steel needle (22 G). The PCL-PCE was electrospun for 6 h at 16 kV (distance from the receiver: 15 cm) to obtain the PCL-PCE as the bottom layer dressing. Spinning solution B was then electrospun for 4 h at 16 kV (distance from the receiver: 15 cm) to obtain the TPU as the dressing by taking a different feed rate intermediate layer; finally, the TPU-HGC was electrospun for 6 h at 17 kV (distance from the receiver: 15 cm) with the bilayer film as the base receiver to obtain the TPU-HGC as the top layer dressing, after the three-layer structure is formed, the 3D BNSF is dried overnight, collected and stored for use. The microfluidic spinning machine (Nanjing Janus New Material Co., LTD.) was used in the whole spinning process.

2.4 Characterization

The microstructure and morphology of particles and nanofibers were observed by scanning electron microscopy (SEM, Hitachi Model SU8010, 3.0 kV accelerating voltage) equipped with an energy-dispersive X-ray spectrum (EDS). Transmission electron microscope (TEM) images of the CF and HGC were obtained using a JEOL JEM-2100 electron microscope at 100 \times magnification and 120 kV acceleration voltage. The functional groups of particles were characterized by using Fourier transform infrared spectrometer (FTIR, Nicolet iS10), over 32 scans in the range from 4000 to 400 cm^{-1} with a resolution of 4 cm^{-1} . The diameters and pore sizes of nanofibers were measured using a capillary flow porometer (CFP-1100AI, Porous Materials Inc). Contact angles of water droplets (5 μL) were measured by the optical contact angle meter system (OCA 20, Data Physics), the image was captured by a high-speed camera after equilibrium for 10 s. The WCA was obtained by measuring the angle between the tangent line of film surface and the droplet baseline. The pressure difference inside and outside the sample was maintained at 100 Pa, and the testing area was 4

cm². These measurements were conducted at 10 randomly selected points to ensure repeatability. The breakthrough pressure of membranes was obtained through measuring the maximum height of water column that the 3D BNSF could support. The water transport behavior of 3D BNSF was characterized using a moisture management tester (MMT, SDL ATLAS). During the test, the sample is placed between two resistive sensor arrays, which measure the resistance on both sides of the membrane, which depends on the water content. Therefore, the water content for the top and bottom surfaces can be calculated by correlation with the corresponding resistances. All tests were repeated at least 5 times. The optical density (OD) values of the bacterial suspension were obtained by a Multiskan GO microplate reader (Thermo Fisher Scientific Co). A wide-mouth bottle was poured into 50 mL DI water and weighed, then completely covered with samples above the mouth, placed at 37 °C with the humidity of 75%. After 24 h, record the weight. The bottle without any membrane was used as a control.

2.5 Colony Assay for the Antimicrobial Activities

The antibacterial ability of 3D BNSF was tested using *S. aureus* and *E. coli*. The bacteria were inoculated into Luria–Bertani (LB) medium and cultured overnight at 37 °C with shaking at 150 r/min until reaching the exponential growth phase. Add 100 µL of bacterial suspension (approximately 1×10^6 mL⁻¹) into a sterilized round 3D BNSF of approximately 1 cm², and incubate at 37 °C and a relative humidity greater than 90%. Use the plate spreading method to inoculate 10 µL of microbial suspension on the LB agar plate. After 24 h of incubation at 37 °C, colony-forming units (CFU) were counted. Pure nanofiber membranes of the same size were used as control samples, and each group was tested three times in parallel. The bacterial viability after contact with the 3D BNSF surface for different times was compared with the number of colonies in the control group. Take 100 µL of *S. aureus* and *E. coli* suspensions ($OD_{\lambda=600}=0.1$) and spread them evenly on the LB medium. Circular 3D BNSF. Samples with a diameter of 1.0 cm were placed on LB medium and cultured at 37 °C for 12 h in an environment with a relative humidity greater than 90%. Then record the diameter of the inhibition zone. Pure nanofiber membranes of the same size were used as control samples, and three parallel experiments were conducted in each group [38].

2.6 In Vitro Cell and in Vitro Wound Healing Experiments

In vitro cell culture: To verify the biocompatibility and cytotoxicity of the three-layer gel-based fiber dressing, NIH 3T3 mouse embryonic fibroblast cells were cultured with

different scaffold samples, and the cell viability was detected using the live-death method. Cells were stained with calcified AM and iodinated PI according to the manufacturer's specifications. The survival status of cells can be observed through a fluorescence microscope. Green fluorescence indicates living cells and red fluorescence indicates dead cells [39].

In vitro wound healing model establishment: A mouse model of infected allograft skin wounds was used to evaluate the effect of a three-layer gel-based fibrous dressing on wound healing. First, 25 healthy male mice (150–230 g, Qilu Hospital, Jinan, China) were selected and divided into 5 groups. Then, a 1 cm × 1 cm skin wound was randomly made on the back of each mouse, and PCL-PCE, PCL, TPU-HGC and 3D BNSF were treated respectively. Images of the wound area were recorded with a digital camera on days 0, 3, 7 and 11. After 11 days, the mice were sacrificed, and the wound granulation tissue was removed and stored in liquid nitrogen for fluorescent immunostaining [40]. All animal experiments were carried out in compliance with the Animal Management Rules of the Ministry of Health of the People's Republic of China and conducted with the approval of Institutional Animal Care. In addition, the experimental protocols were approved by the Animal Ethics Committee of Shandong University (SYXK(Lu)20,230,049) and the Health Guide for the Care and Use of Laboratory Animals of National Institutes.

3 Results and Discussion

3.1 Analyses of HGC and PCE

FTIR spectral features, including components, modifications, and interactions, offer valuable insights into material chemistry [41]. Figure 2a shows the FTIR spectra of GA, CF, GA-CF, and HGC. In the GA spectrum, the stretching vibration and hydrogen bond absorption peaks of the phenolic hydroxyl group (–OH) are evident at 3494 and 3284 cm⁻¹, respectively. The absorption at 1030 cm⁻¹, representing the C–O stretching vibration, serves as an internal standard. The amide II absorption at 1560 cm⁻¹ indicates partial deacetylation. Compared with the absorption ratio of A1560/A1030, the ratio of GA-CF was 1.0124, while that of CF was 1.0617, suggesting partial removal of the acetyl group at the C2 position of CF. Upon GA-CF formation, the absorption intensity at these positions decreases, with a new peak emerging at approximately 3440 cm⁻¹, indicating strong intermolecular hydrogen bonding between GA and CF, promoting their combination to form GA-CF particles. In the FTIR spectrum of HGC, two peaks (2919 and 2851 cm⁻¹) from GA-CF are clearly inherited, along with new peaks (1467 and 721 cm⁻¹), suggesting the presence of

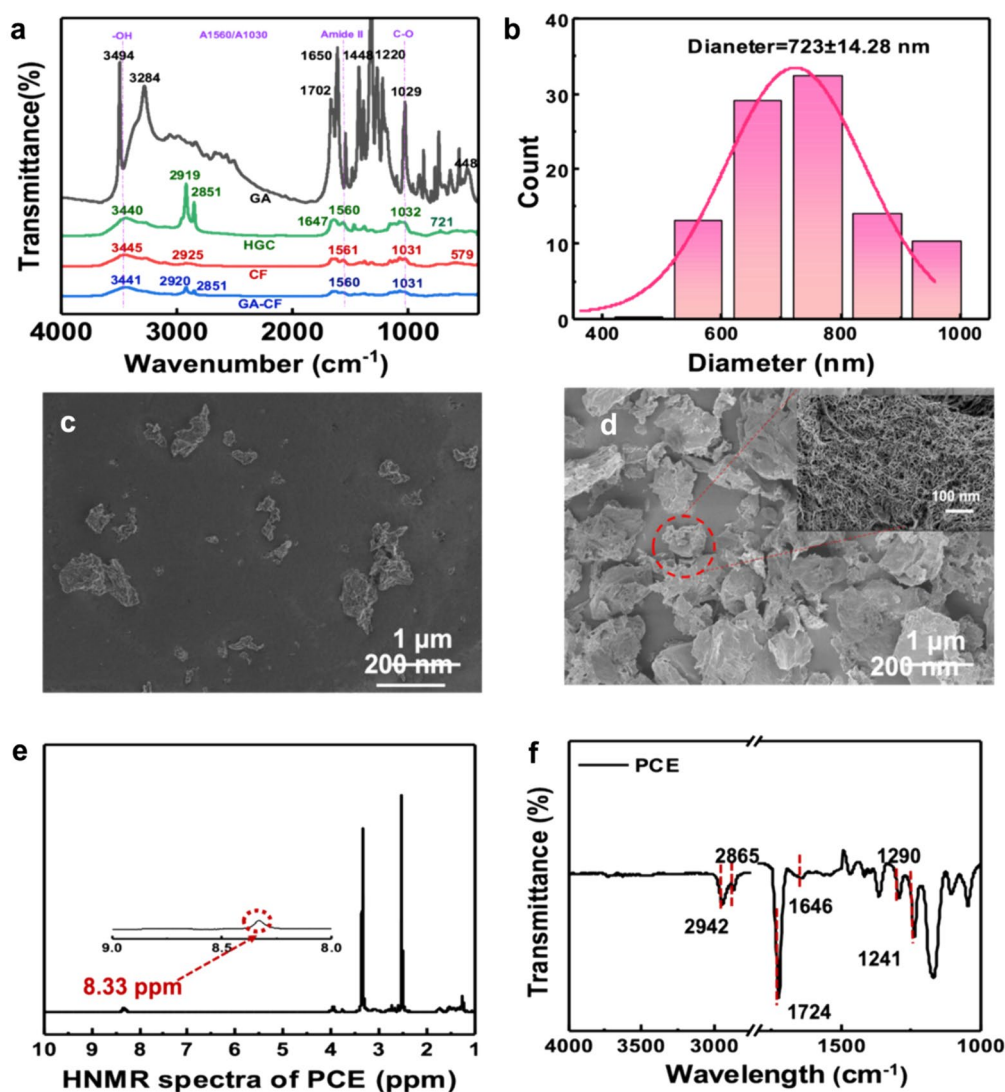


Fig. 2 Characterization of the structure and properties of HGC particles. **a** FT-IR spectra of CF, GA-CF and HGC; **b** Particle size distribution of HGC particles; **c**, **d** SEM images of CF and HGC particles; **e** HNMR analysis of PCE; **f** FTIR spectra of PCE

hydrophobic substances. These results collectively support successful HGC particle preparation.

The acetylation level of nano-chitin was assessed by utilizing the ratio of methyl carbon integration to the integration of carbons 1 through 5, yielding a value of 0.93. Following subsequent deacetylation treatment, this level decreased to 0.88, indicating an effective reduction in acetylation. Furthermore, the chemical shift of the carbon in the C=O moiety shifted from 174.28 ppm after 173.60 ppm after deacetylation (Fig. S2-3). This shift is attributed to changes in the chemical environment of the carbonyl carbon after deacetylation, resulting in weakened electron-withdrawing effects and an overall upfield shift in the chemical shift.

Measurements were conducted to determine the average particle size of the HGC particles. As depicted in Fig. 2b, the particle size distribution ranges from 500 to 1000 nm,

with the majority of the particles falling within the range of 600–800 nm. The larger particle size is attributed to significant agglomeration between GA-CF. The activation behavior of GA on the surface of CF enhances the entanglement between these components, resulting in the formation of larger particles.

Superhydrophobic surfaces typically feature micro/nanostructures that create an air layer, establishing an interface between water molecules and the surface and effectively preventing water penetration [42, 43]. SEM analysis of the superhydrophobic particles revealed their micro/nanoprotuberant structure (Fig. 2c). Notably, the interior of the HGC particles was densely packed with nanofibers (Fig. 2d), contributing to increased surface roughness. This roughness arises from nanofiber aggregation or entanglement during the GA-CF

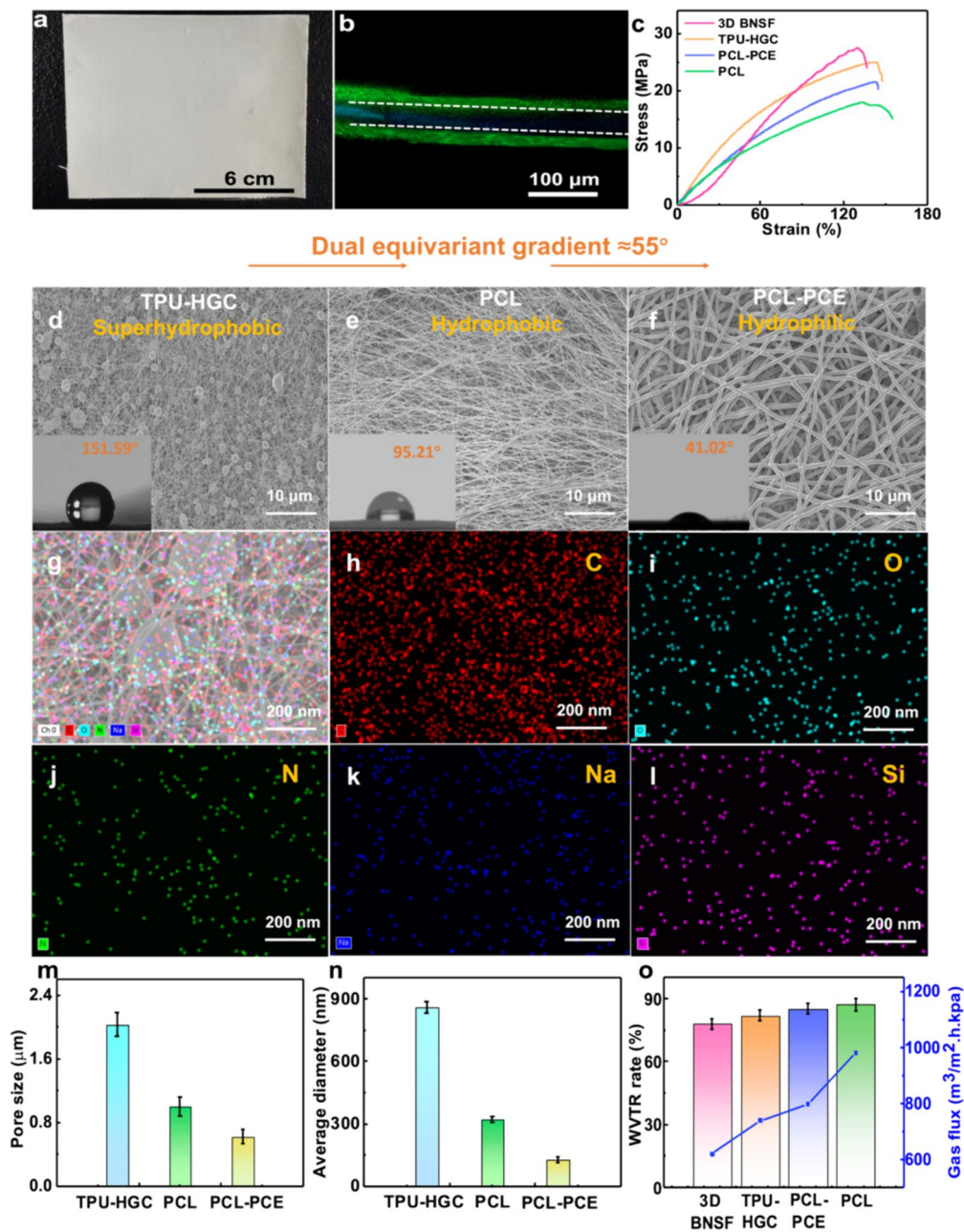


Fig. 3 Characterization of the structure and properties of 3D BNSF. **a** Photographic image of a 3D BNSF. **b** Element mappings of the cross-section of 3D BNSF. Scale bar: 100 μm . **c** Tensile stress–strain curves of the different layers at a stretching rate of 0.2 mm/s. **d–f**

SEM and water contact angle images of TPU-HGC (**d**), PCL (**e**), and PCL-PCE (**f**). **g–i** Micromorphology and elemental distribution of 3D BNSF. **m, n** Pore size and average diameter of TPU-HGC, PCL-PCE, and PCL. **o** WVTR and gas flux performance of different groups

preparation process, which is driven by hydrogen bonding forces.

High nuclear magnetic resonance (HNMR) analysis was utilized to determine the chemical structure of the biomimetic elastomer PCE [44] (Fig. 2e). (Fig. 2e). The figure illustrates that PCE is synthesized through a grafting reaction between PC and EPL. The successful synthesis of PCE was confirmed by the presence of a minor

peak at 8.59 ppm ($-\text{CO}-\text{NH}-$) in the nuclear magnetic resonance spectrum, which verified its chemical structure. Additionally, FTIR analysis of the PCE revealed characteristic absorption peaks at 2942 cm^{-1} and 2865 cm^{-1} , corresponding to the vibrations of $-\text{CH}_3$ and $-\text{CH}_2$, respectively. The peaks at 1724 cm^{-1} and 1646 cm^{-1} are attributed to the stretching vibrations of the $\text{C}=\text{O}$ and $\text{CO}-\text{NH}$ functional groups, respectively. Moreover, the peaks observed

at 1290 cm^{-1} and 1241 cm^{-1} are linked to the C–O–C functional group (Fig. 2f). Both nuclear magnetic resonance and infrared analyses confirmed the successful preparation of the biomimetic elastomer PCE.

3.2 Characterization of the Structure and Properties of the 3D BNSF

The 3D BNSF dressing, obtained through micro-electro-spinning of PCL-PCE, PCL, and TPU-HGC nanofibers, demonstrated scalability and integrity (Fig. 3a and Fig. S4). Elemental mappings of the 3D BNSF confirmed their three-layered structure (Fig. 3b). Furthermore, 3D BNSF exhibited a tensile strength of 27 MPa at an elongation ratio of 130%, indicating strong elasticity against elongation. Details of the

tensile property test are provided in Text S1. Compared to PCL or PCL-PCE, 3D BNSF exhibits notable elongation and enhanced mechanical strength due to the addition of layered TPU-HGC fibrous textiles (Fig. 3c and Fig. S5). SEM images of the superhydrophobic layer of TPU-HGC, the hydrophobic layer of PCL, and the hydrophilic layer of PCL-PCE are shown in Fig. 3d–f. The three layers consist of fibrous membranes with varying pore sizes and diameters. Additionally, SEM and EDS images (Fig. 3g–i) reveal numerous fiber-granule complexes on the surface of TPU-HGC, accompanied by the presence of C, N, O, Na, and Si, as described in Fig. 1a.

Additionally, the water contact angles for TPU-HGC, PCL, and PCL-PCE were 151.59° , 95.21° , and 41.02° (Fig. 3d–f, Fig. S6 and Text S2), respectively. These values

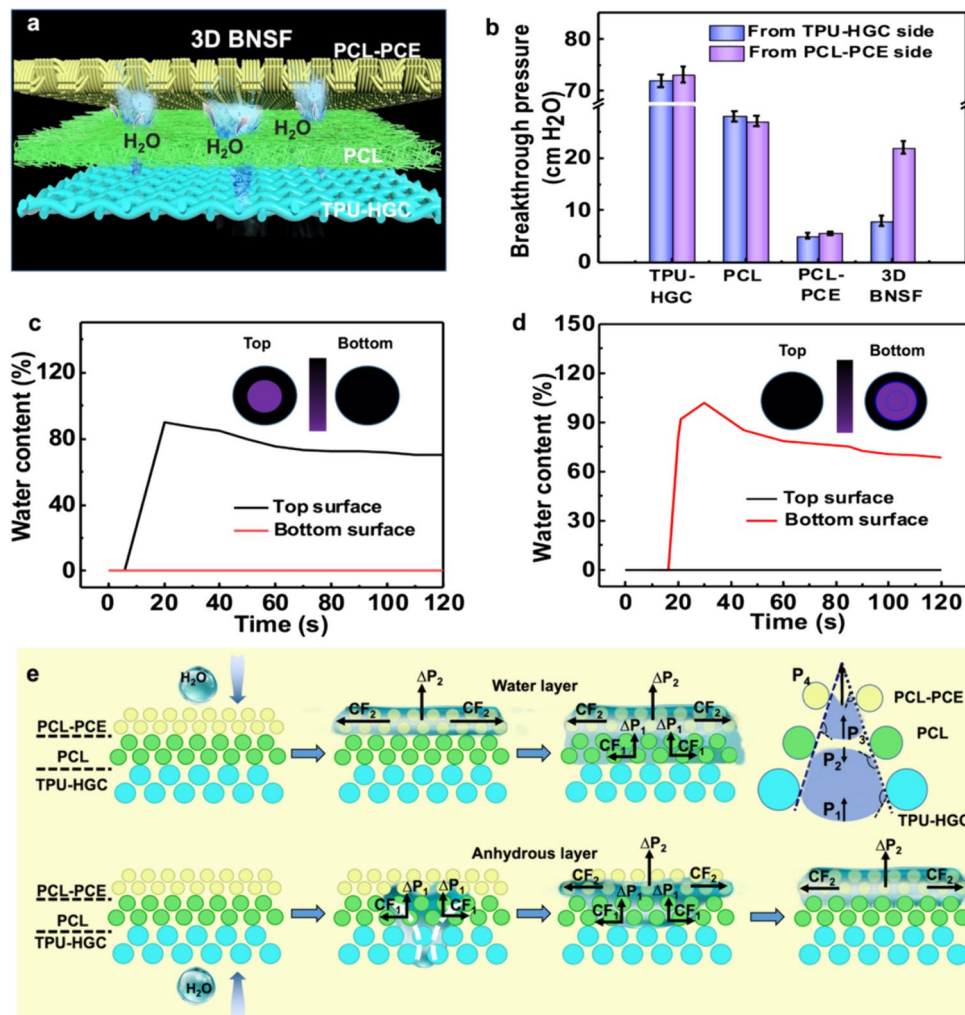


Fig. 4 Demonstration and characterization of the unidirectional fluid draining capability of the 3D BNSF. **a** Schematic showing unidirectional water transport across the 3D BNSF; **b** Anisotropic breakthrough pressure of different NSF, indicating that 3D BNSF permits only unidirectional water movement; **c–d** MMT results showing the

relative water content of the top and bottom surfaces of 3D BNSF when the PCL-PCE and TPU-HGC groups were facing, respectively. **e** Diagrams showing the simplified mechanism of the passive wicking process of 3D BNSF (the inset shows the process in the vertical direction)

indicate the successful creation of 3D BNSF with a dual equivariant gradient of superhydrophobic-hydrophobic-hydrophilic properties (the difference in the water contact angle between interfaces is approximately 55°). This gradient contributes to maintaining the biofluid transfer rate of 3D BNSF and a low humidity environment on the wound surface. The superhydrophobic characteristic of TPU-HGC arises from the combination of HGC and TPU, resulting in a substantial increase in the water contact angle from 131.58° to 151.48° (Fig. S7).

The pore sizes and fiber diameters of the three types of fibrous layers were examined, as illustrated in Fig. 3m and n. The analysis revealed that TPU-HGC has an average fiber diameter of $2.79\ \mu\text{m}$ and an average pore size of $13\ \mu\text{m}$ (macrosized pores), which is significantly larger than that of PCL, which has a pore size of $3.8\ \mu\text{m}$ (micron-sized pores). Additionally, PCL-PCE exhibited the smallest fiber diameter of $0.19\ \mu\text{m}$ and a pore size of $0.97\ \mu\text{m}$ (submicron-sized pores) (Fig. S8). These findings highlight the hierarchical multiscale porous structure of 3D BNSF. Concerning the wetting effect, the various layers of 3D BNSF demonstrate an increasing water absorption tendency from the inner layer to TPU-HGC (Fig. S9 and Text S3). The breathability of the wound dressing, another essential feature for comfort, is evaluated through a water vapor transmission (WVT) rate assessment [42, 43]. The optimized 3D BNSF exhibited a relatively high WVT of 78% and a gas flux of $620\ \text{m h}^{-1}\ \text{kPa}^{-1}$ (Fig. 3o).

3.3 Highly Efficient and Unidirectional Water Transport Mechanism Model of the 3D BNSF

To show the highly effective and one-way drainage capability of the 3D BNSF from TPU-HGC to the inner layer (Fig. 4a), we devised a simplified physical model involving a continuous flow of violet ink droplets dripping from a syringe, mimicking an exuding wound. We measured the breakthrough pressures of the 3D BNSF from both the inner to outer side direction and the reverse direction. As the layer transitions from superhydrophobic to hydrophobic and finally to hydrophilic, the breakthrough pressures of TPU-HGC, PCL, and PCL-PCE decrease from $> 70\ \text{mm H}_2\text{O}$ to $< 10\ \text{mm H}_2\text{O}$, as depicted in Fig. 4b. This decrease is attributed to a reduction in surface energy. However, the prepared 3D BNSF exhibits a significantly lower breakthrough pressure from the inner side direction, amounting to 32% of the reverse breakthrough pressure at $22\ \text{mm H}_2\text{O}$, showing a remarkable directional water transport performance. Additionally, the hydrophobic TPU-HGC of the 3D BNSF halts water transport once the hydrostatic pressure drops below $7\ \text{mm H}_2\text{O}$, effectively preventing dehydration of the surrounding tissue.

Additionally, the directional water transport performance was quantitatively assessed to determine the high efficiency of water transportation. Figure 4c, d shows the changes in the relative water content on both sides of the biomimetic 3D BNSF when the samples were laid horizontally while saline water was vertically dripped onto the TPU-HGC (Fig. 4c) and the PCL-PCE (Fig. 4d), respectively. Interestingly, the water content of TPU-HGC rapidly decreased to 0 within 20 s, while the water concentration of PCL-PCE reached equilibrium when TPU-HGC was facing, which is considered the top side. This phenomenon occurred due to the increased capillary force in the PCL-PCE, resulting from its hierarchical multiscale porous structure, which effectively pulled water away from the TPU-HGC [45–47]. In contrast, the water content of TPU-HGC remains almost negligible when PCL-PCE is positioned downward, suggesting that water cannot penetrate through TPU-HGC. Additionally, the insets in Fig. 4c and 4d illustrate the dry (dark) and wet (blue) regions on both sides, indicating that water is primarily concentrated within the PCL-PCE. This suggests that the prepared 3D BNSF exhibits impressive and highly efficient directional water transport performance.

To further demonstrate the directional water transport abilities of both the monolayer and 3D BNSF, we conducted an experiment by spreading $50\ \mu\text{L}$ of violet ink droplets onto their surfaces (Fig. S10 and Text S4). The outcomes clearly illustrate that TPU-HGC exhibited minimal changes within 200 s and did not demonstrate any wetting behavior. In contrast, PCL-PCE began to infiltrate at 10 s and was entirely wetted by the violet ink droplets at 200 s. This observation validates that the 3D BNSF displayed effective directional water transport properties. As shown in Fig. S11, the surface's superhydrophobic characteristics effectively hindered the rapid wetting of the violet ink droplets, indicating the successful prevention of undesired water infiltration by the 3D BNSF.

When droplets encounter fiber membranes, they typically penetrate the capillary channels within the fibers, experiencing Laplace pressure ($P = 4\gamma \cdot \cos\theta / D$). Here, γ represents the liquid–gas interfacial tension ($0.072\ \text{N m}^{-1}$ for water at $25\ ^\circ\text{C}$), θ is the contact angle on the fiber surface, and D is the fiber pore size [48, 49]. This passive water absorption process is demonstrated using a vertebral model (Fig. 4e) [50]. The Laplace pressure of a droplet within a capillary tube fluctuates due to variations in water contact angles and pore sizes across the outer, transport, and TPU-HGC layers [51, 52]. Sweat traverses the skin surface into internal capillary channels [53–56]. At the junction of TPU-HGC and the transport layer, the fluid encounters two Laplace pressures, P_1 and P_2 , acting in the same direction, resulting in an upward Laplace pressure difference $\Delta P = 4\gamma \cdot \cos\theta_2 / D_2 - 4\gamma \cdot \cos\theta_1 / D_1 = P_2 - |P_1|$, where θ_1 denotes the water contact

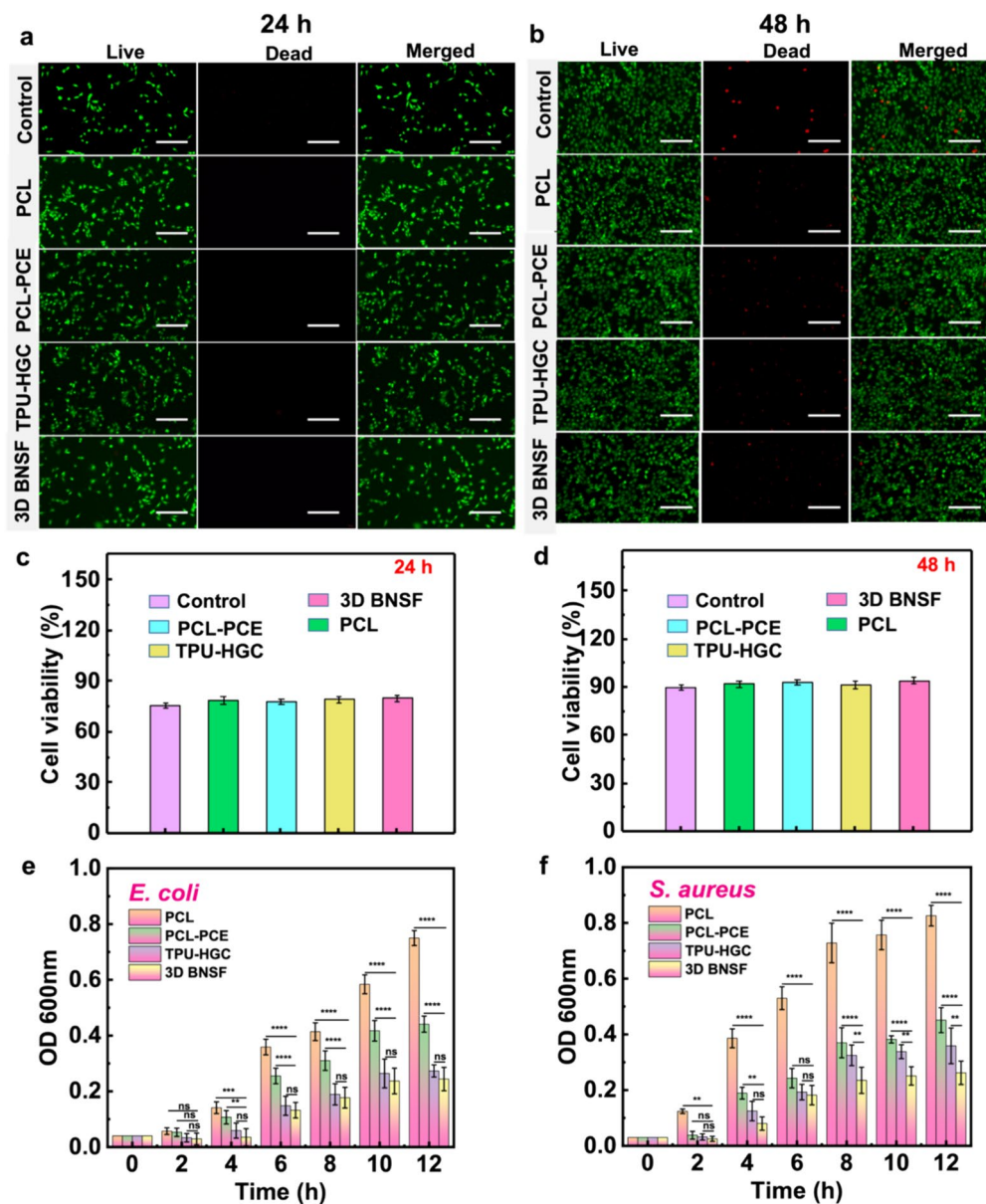


Fig. 5 a, b Fluorescence viability of live/dead cells in different groups (24 h and 48 h). Scale bar, 80 μ m; c, d Cell viability in different groups after incubation for 24 h and 48 h; e, f Quantitative analysis of the antibacterial performance of PCL, PCL-PCE, TPU-HGC and 3D BNSF

angle in TPU-HGC and θ_2 represents that on the transport layer [57, 58]. Similarly, the Laplace pressure difference at the interface of the transport layer and PCL-PCE can be expressed as $\Delta P_2 = P_4 + |P_3|$, with a similar upward direction. Thus, the forces exerted on the liquid during motion are perpendicular [59, 60].

3.4 Antimicrobial Performance and Biocompatibility of the 3D BNSF

Biocompatibility testing and antimicrobial property analysis were employed to determine whether 3D BNSF can be

safely used in living organisms without resulting in detrimental reactions, including inflammation, infection, and/or toxicity. Thus, we incubated NIH/3T3 fibroblasts with PCL, PCL-PCE, TPU-HGC, and 3D BNSF. After incubation for 24 h and 48 h, AM/PI fluorescence imaging was employed to separately label live and dead cells. Cells emitting green fluorescence were considered live cells, while those emitting red fluorescence were considered dead cells. The live/dead cell fluorescence imaging maps clearly demonstrated that all four groups (PCL-PCE, PCL, TPU-HGC, and 3D BNSF) exhibited remarkable biocompatibility following coculture. Figure 5a, b displays the cell survival rates for the

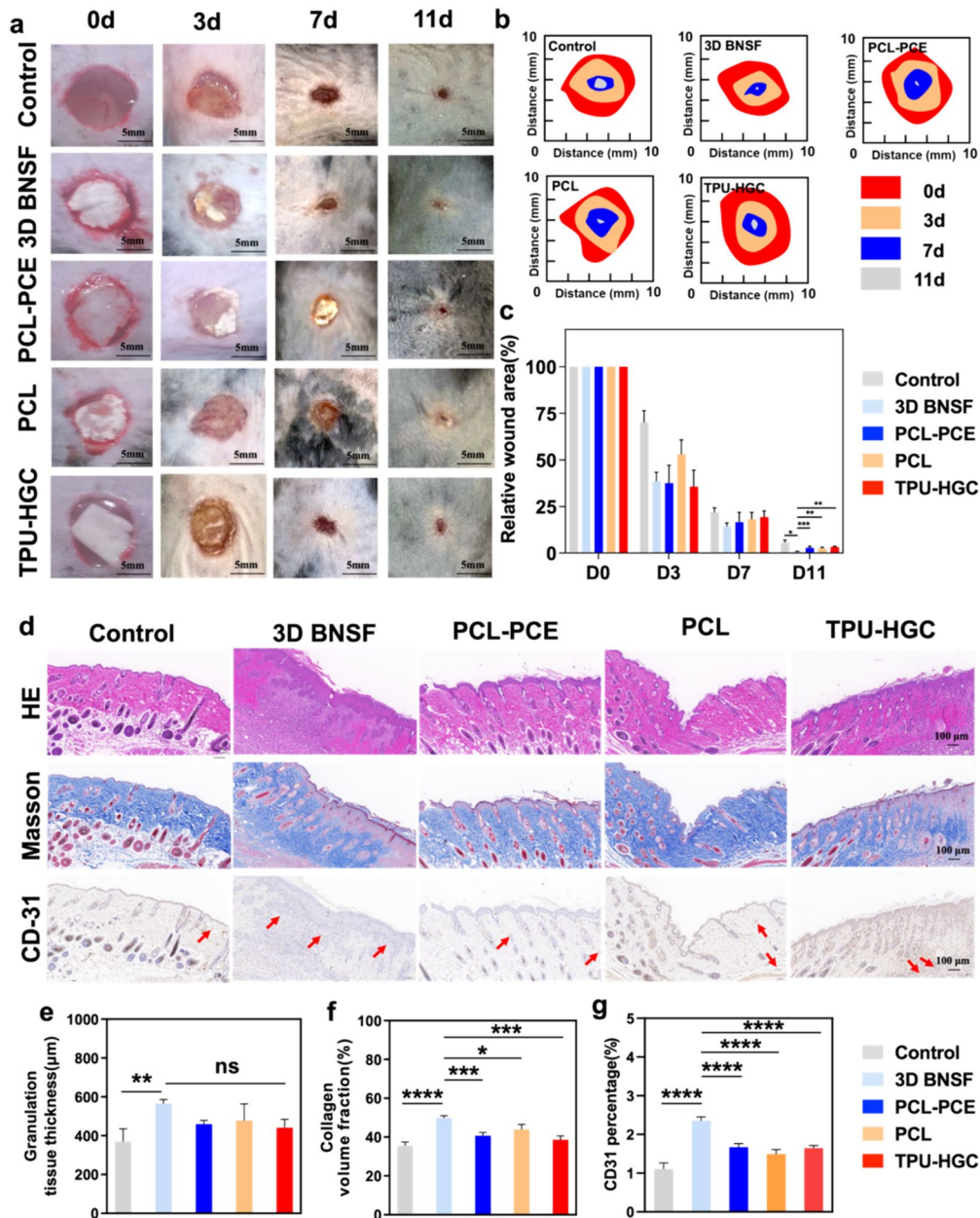


Fig. 6 **a** Representative images tracking wound closure over 11 days. **b** Schematic images of wound contraction over 11 days. **c** Quantitative wound area variations for each group on different days. **d** H&E staining (scale bar: 100 µm), CD31 immunostaining (scale bar:

100 µm), and Masson staining (scale bar: 100 µm) of wound tissues after different treatments on day 11. **e–g** Quantitative analysis of the granulation thickness, collagen volume fraction and CD31 percentage in the five groups

five groups. Clearly, the cell survival rates for the PCL-PCE, PCL, TPU-HGC, and 3D BNSF dressings were approximately 90%. The 48 h graph shows a clear difference compared to the 24 h data. This is consistent with the live/dead images, which show an increase in the number of live cells after 48 h, indicating that cell proliferation has occurred. The cell survival rate of the 3D BNSF group was marginally greater than that of the other control groups (Fig. 5c,

d). Based on these results, it can be concluded that the 3D BNSF dressing possesses exceptional biocompatibility.

3D BNSF, which functions as a multifunctional dressing, prevents external toxic substances from reaching the surface of skin wounds due to the presence of a superhydrophobic structure on its top layer [61–63]. Furthermore, self-synthesized superhydrophobic particles demonstrate a degree of antibacterial activity [64–66]. Thus, two approaches were

utilized to assess its inhibitory effect on two prevalent bacteria, *S. aureus* and *E. coli*.

The antimicrobial activity of 3D BNSF was further confirmed by bacterial regrowth curves using OD 600 measurements. Figure 5e, f shows the OD growth curves of *E. coli* and *S. aureus* suspensions incubated with different nanofibers. The bactericidal activity increased in the order of PCL, PCL-PCE, TPU-HGC, and 3D BNSF. As depicted in Fig. 5e, the growth trend of *E. coli* incubated with PCL was notably greater than that of the other groups, suggesting that PCL exhibits almost no antimicrobial activity. Conversely, TPU-HGC and 3D BNSF significantly suppressed the growth of *E. coli*. The potent antimicrobial efficacy of 3D BNSF was further evidenced by its culture with *S. aureus*, where colony growth was markedly slow after 12 h of coculture with both bacteria. In contrast to the remarkable antimicrobial properties of 3D BNSF, the presence of PCL appeared to stimulate the growth of both *E. coli* and *S. aureus*. As shown in Fig. 5f, initially, the growth pattern of *S. aureus* cultured with PCL resembled that shown in Fig. 5e, but it notably accelerated after 6 h of incubation. This suggests a greater bacterial presence in the PCL, possibly due to its superior biocompatibility. Upon examination, the relatively lower optical density of the supernatant in the PCL-PCE could be attributed to bacterial adsorption on the nanofibers [67, 68]. Similarly, the lower OD values of TPU-HGC and 3D BNSF might be due to the inherent antimicrobial properties of HGC.

3.5 Rat Wound Observation and Histological Analysis in Rats

We conducted a study using a rat full-thickness abdominal wall defect model to investigate the effect of 3D BNSF dressings on wound healing [69]. Additionally, we examined the impact of electrostatically spun fiber membrane dressings on wounds using the same model. Circular full-thickness notches (diameter: 8 mm) were created on the backs of the rats, and PCL, PCL-PCE, TPU-HGC, and 3D BNSF were applied to the defects. Images of the wounds were captured on days 3, 7, and 11 to assess the wound area (Fig. 6a). On day 3, the control group exhibited unsatisfactory wound results with exudates, while the other four groups showed wounds without exudates. The wound area of the 3D BNSF group was smaller than that of the other groups, indicating superior exudate absorption and drainage efficacy. By day 7, the wound area associated with the 3D BNSF was further reduced, suggesting its ability to promote wound repair.

As depicted in the wound images, contours, and wound areas shown in Fig. 6b and c, wound healing was markedly accelerated in the 3D BNSF group compared to the other four groups. By the 7th day, the wound area in the 3D BNSF group had decreased by 86%. In contrast, the

wound areas of the patients in the PCE-PCL, PCL, and TPU-HGC groups decreased by 83%, 81.7%, and 80.7%, respectively. By the 11th day, the wounds in the 3D BNSF group had nearly completely healed, with skin regeneration (skin defect area, 0.84%). 3D BNSF integrates precise control over material composition and nanofiber alignment, achieving an exact distribution of superhydrophobic, hydrophobic, and hydrophilic gradients. Compared to traditional nanofiber scaffolds, it maintains a greater wound healing rate at approximately 11 days [69–71]. Moreover, the wound areas of the control, PCE-PCL, PCL, and TPU-HGC groups healed by 93.06%, 96.49%, 97.03%, and 96.35%, respectively. The remarkable healing-promoting effect of the 3D BNSF dressing can be attributed to its composition primarily consisting of biomass, which creates an optimal wound healing environment [72, 73]. Additionally, the impressive healing-promoting effect of 3D BNSF is attributed to its dual equivariant gradient properties, which promote cell proliferation and accelerate wound healing [71].

A histological evaluation of an in vivo study utilizing a full-thickness skin defect model demonstrated that 3D BNSF significantly accelerated wound healing. This finding aligns with recent studies emphasizing the importance of advanced scaffold materials in enhancing tissue repair processes. Specifically, the impact of 3D BNSF on granulation tissue formation and collagen deposition represents a notable advancement in wound healing technology [74]. Histological examination of HE-stained tissue sections revealed that the 3D BNSF group had thicker regenerating granulation tissue than did the positive control group, PCE-PCL, PCL, and TPU-HGC (Fig. 6d and Fig. S12). On day 11, granulation dermal tissue (GDT) analysis showed that the 3D BNSF group achieved a GDT percentage of 564.63%, surpassing that of the positive controls (369.35%), PCE-PCL (459.22%), and PCL (478.05%) (Fig. 6e). This indicates a substantial enhancement in tissue regeneration. Previous studies have reported similar trends, but the extent of improvement with 3D BNSF is more pronounced, likely due to its unique structural and material properties that better mimic the extracellular matrix and provide a conducive environment for cell proliferation and tissue growth.

Mason's trichrome staining was used to assess collagen deposition, a critical factor in wound healing. Collagen appeared blue, while myofibers appeared red. The 3D BNSF group exhibited greater collagen volume and deposition (49.75%) than did the positive control (35.46%), PCE-PCL (40.71%), and PCL (43.98%) groups (Fig. 6d, f). This substantial increase in collagen deposition by day 11 suggested that 3D BNSF effectively promoted ECM formation and remodeling. This finding contrasts with some previous studies where the increase in collagen deposition was less significant, highlighting the superior performance of 3D BNSF in accelerating the wound healing process. The angiogenic potential of 3D

BNSF was evaluated using CD31 staining to assess new blood vessel formation (Fig. 6d, g and Fig. S12). Although there was no significant difference in the number of new blood vessels among the single-layer groups, the 3D BNSF group showed a markedly greater percentage of neovascularization. This indicates that 3D BNSF effectively promotes angiogenesis, likely due to the reduced immune response from the antibacterial properties of HGC particles in 3D BNSF and its ability to enhance blood vessel formation by effectively resisting bacterial infection, a critical process in wound healing [75]. The enhanced angiogenesis observed in this study is consistent with recent research.

4 Conclusion

In summary, a 3D BNSF featuring dual equivariant gradient traits, robust antimicrobial properties, and favorable biocompatibility was designed to effectively seal wounds and expedite skin wound recovery. This study revealed that the multilayered nanofiber architecture confers strong mechanical resilience and unidirectional fluid transport abilities to 3D BNSF. Additionally, the inherent antimicrobial attributes, composite structure, and superhydrophobicity of HGC collectively improve the antimicrobial efficacy of 3D BNSF, aiding in efficient wound closure and significant enhancement of wound healing. Additionally, 3D BNSF swiftly absorbs moisture within a short timeframe, keeping skin wounds dry through unidirectional fluid transport with dual-gradient properties. Moreover, the 3D BNSF promoted granulation tissue formation and collagen deposition, further promoting wound healing. With these promising attributes, 3D BNSF has emerged as promising candidates for animal and human wound treatment strategies, offering wide-ranging potential applications in relevant biomedical domains.

Supplementary Information The online version contains supplementary material available at <https://doi.org/10.1007/s42765-024-00476-8>.

Acknowledgements This work was supported by the National Natural Science Foundation of China (22278225), National Key Research and Development Program of China (2018YFC1602800), China Postdoctoral Science Foundation (2022M712180), Natural Science Foundation of Fujian Province (2022J02021).

Author contributions Lin Wang: Conceptualization, data curation, software, validation, formal analysis, writing original draft. Tengxiao Huang: Conducted most of the animal experiments, formal analysis. Xiaowei Xu, Nitong Bu and Zhenzhen Wu: Methodology, data curation. Yunpeng Zhao: Conducted most of the animal experiments, formal analysis. Ya-Qin Zhou: Methodology, data curation. Su Chen: Writing—review & editing. Yong Chen: Writing—review & editing. Jie Pang: Funding acquisition, supervision, writing—review & editing.

Data availability The data that support the findings of this study are available from the corresponding author upon reasonable request.

Declarations

Conflict of interest The authors declare no conflict of interest.

References

1. Tang TN, Nguyen TH, Tran CM, Doan VK, Nguyen NTT, Vu BT, Dang NNT, Duong TT, Pham VH, Tran LD, Vo TV, Nguyen TH. Fabrication of silver nanoparticle-containing electrospun polycaprolactone membrane coated with chitosan oligosaccharides for skin wound care. *J Sci-adv Mater Dev.* **2023**;8:100582.
2. Pang Q, Yang F, Jiang ZL, Wu KH, Hou RX, Zhu YB. Smart wound dressing for advanced wound management: real-time monitoring and on-demand treatment. *Mater Des.* **2023**;229: 111917.
3. Li Y, Zhang Y, Wang YX, Yu K, Hu EL, Lu F, Shang SM, Xie RQ, Lan GQ. Regulating wound moisture for accelerated healing: a strategy for the continuous drainage of wound exudates by mimicking plant transpiration. *Chem Eng J.* **2022**;429: 131964.
4. Barros NR, Ahadian S, Tebon P, Rudge MVC, Barbosa AMP, Herculano RD. Highly absorptive dressing composed of natural latex loaded with alginate for exudate control and healing of diabetic wounds. *Mat Sci Eng C-Mater.* **2021**;119: 111589.
5. Satish A, Aswathi R, Caroline Maria J, Sai KP. Triiodothyronine impregnated alginate/gelatin/polyvinyl alcohol composite scaffold designed for exudate-intensive wound therapy. *Eur Polym J.* **2019**;110:252.
6. Zou F, Wang YS, Tang T, Zheng YD, Xie Y, Zhu SH, Yang HY, Meng HY, Liu XD, Yang JY. Synergistic strategy constructed hydrogel-aerogel biphasic gel (HAB-gel) with self-negative-pressure exudate absorption, M2 macrophage-polarized and antibacterial for chronic wound treatment. *Chem Eng J.* **2023**;451: 138952.
7. Giovannini GG, Cinelli P, Boesel L, Rossi RM. Thioflavin-modified molecularly imprinted hydrogel for fluorescent-based non-enzymatic glucose detection in wound exudate. *Mater Today Bio.* **2022**;14: 100258.
8. Halder M, Narula M, Singh Y. Supramolecular, nanostructured assembly of antioxidant and antibacterial peptides conjugated to naproxen and indomethacin for the selective inhibition of COX-2, biofilm, and inflammation in chronic wounds. *Bioconjugate Chem.* **2023**;34:645–63.
9. Yuan Y, Fan DD, Shen SH, Ma XX. An M2 macrophage-polarized anti-inflammatory hydrogel combined with mild heat stimulation for regulating chronic inflammation and impaired angiogenesis of diabetic wounds. *Chem Eng J.* **2022**;433: 133859.
10. Wang K, Wang JH, Li L, Xu LQ, Feng N, Wang Y, Fei X, Tian J, Li Y. Synthesis of a novel anti-freezing, non-drying antibacterial hydrogel dressing by one-pot method. *Chem Eng J.* **2019**;372:216.
11. Lan JZ, Shi LX, Xiao WY, Zhang XB, Wang ST. A rapid self-pumping organohydrogel dressing with hydrophilic fractal microchannels to promote burn wound healing. *Adv Mater.* **2023**;35:2301765.
12. Jia XL, Hua C, Yang FB, Li XX, Zhao P, Zhou FF, Lu YC, Liang H, Xing M, Lyu GZ. Hydrophobic aerogel-modified hemostatic gauze with thermal management performance. *Bioact Mater.* **2023**;26:142.
13. Li HB, Dai JL, Yi XT, Cheng F. Generation of cost-effective MXene@polydopamine-decorated chitosan nanofibrous wound dressing for promoting wound healing. *Mat Sci Eng C-Mater.* **2022**;140: 213055.
14. Xiao WY, Wan XZ, Shi LX, Ye MS, Zhang YK, Wang ST. A viscous-biofluid self-pumping organohydrogel dressing to accelerate diabetic wound healing. *Adv Mater.* **2024**;29:2401539.

15. Huang HY, Dong ZC, Ren XY, Jia B, Lie GW, Zhou SW, Zhao X, Wang WZ. High-strength hydrogels: fabrication, reinforcement mechanisms, and applications. *Nano Res.* **2023**;16:3475–515.
16. Jia B, Huang HY, Dong ZC, Ren XY, Lu YY, Wang WZ, Zhou SW, Zhao X, Guo BL. Degradable biomedical elastomers: paving the future of tissue repair and regenerative medicine. *Chem Soc Rev.* **2024**;53:4086.
17. Jia B, Dong Z, Ren X, Niu M, Kong S, Wan X, Huang H. Hydrogels composite optimized for low resistance and loading–unloading hysteresis for flexible biosensors. *J Colloid Interface Sci.* **2024**;671:516.
18. Dong ZC, Ren XY, Jia B, Zhang XJ, Wan XP, Wu Y, Huang HY. Composite patch with negative Poisson's ratio mimicking cardiac mechanical properties: design, experiment and simulation. *Mater Today Bio.* **2024**;26: 101098.
19. Yin J, Xu L, Ahmed A. Batch preparation and characterization of electrospun porous polylactic acid-based nanofiber membranes for antibacterial wound dressing. *Adv Fiber Mater.* **2022**;4:832.
20. Luo Z, Jiang L, Xu CF, Kai D, Fan XS, You ML, Hui CM, Wu CS, Wu YL, Li ZB. Engineered Janus amphiphatic polymeric fiber films with unidirectional drainage and anti-adhesion abilities to accelerate wound healing. *Chem Eng J.* **2021**;421: 127725.
21. Pi HH, Xi YL, Wu J, Hu MM, Tian BY, Yang YW, Wang R, Zhang XQ. Janus fibrous membrane with directional liquid transport capacity for wound healing promotion. *Chem Eng J.* **2023**;455: 140853.
22. Li TT, Sun L, Zhang Y, Shiu BC, Ren HT, Peng HK, Lin JH, Lou CW. Chitosan-based antibacterial microspheres loaded multifunctional Janus composite membranes with unidirectional biofluid transport, antioxidant and pH-responsive monitoring. *Chem Eng J.* **2023**;472: 144820.
23. Su Y, Mainardi V, Wang H, McCarthy A, Zhang Y, Chen SX, John J, Wong S, Hollins R, Wang GS, Xie JW. Dissolvable microneedles coupled with nanofiber dressings eradicate biofilms via effectively delivering a database-designed antimicrobial peptide. *ACS Nano.* **2020**;14:11775.
24. Wang L, Mu RJ, Li YZ, Lin LZ, Lin ZY, Pang J. Characterization and antibacterial activity evaluation of curcumin loaded konjac glucomannan and zein nanofibril films. *Lwt-Food Sci Technol.* **2019**;113: 108293.
25. Liang YQ, Liang YP, Zhang HL, Guo BL. Antibacterial biomaterials for skin wound dressing. *Asian J Pharm Sci.* **2022**;17:353.
26. Pan F, Giovannini GG, Zhang SX, Altenried SF, Zuber F, Chen Q, Boesel L, Ren Q. pH-responsive silica nanoparticles for the treatment of skin wound infections. *Acta Biomater.* **2022**;145:172.
27. Homaeigohar S, Boccaccini A. Antibacterial biohybrid nanofibers for wound dressings. *Acta Biomater.* **2020**;107:25.
28. Mirani B, Hadisi Z, Pagan E, Dabiri SMH, van Rijt A, Almutairi L, Noshadi I, Armstrong D, Akbari M. Smart dual-sensor wound dressing for monitoring cutaneous wounds. *Adv Healthcare Mater.* **2023**;12:2203233.
29. Liu L, Sun HQ, Zhang JM, Xu BJ, Gao YJ, Qi DM, Mao ZW, Wu JD. Trilayered fibrous dressing with wettability gradient for spontaneous and directional transport of massive exudate and wound healing promotion. *Adv Fiber Mater.* **2022**;5:574.
30. Huang WC, Ying R, Wang W, Guo YN, He YJ, Mo XY, Xue CH, Zhao MX. A macroporous hydrogel dressing with enhanced antibacterial and anti-inflammatory capabilities for accelerated wound healing. *Adv Funct Mater.* **2020**;30:2000644.
31. Qi LY, Ou KK, Hou Y, Yuan PP, Yu W, Li X, Wang BX, He J, Cui SZ, Chen XG. Unidirectional water-transport antibacterial trilayered nanofiber-based wound dressings induced by hydrophilic-hydrophobic gradient and self-pumping effects. *Mater Des.* **2021**;201: 109461.
32. Chen F, Tian QR, Wang T, Ma LL, Liu RF, Wang S. Fabrication of a multifunctional antibacterial Cotton-based fabric for personal cooling. *Appl Surf Sci.* **2023**;609: 155291.
33. Ding SP, Zhang TH, Wu MM, Wang XF. Photothermal dual-layer hydrophilic/hydrophobic composite nanofibrous membrane for efficient solar-driven membrane distillation. *J Membr Sci.* **2023**;680: 121740.
34. Tang Y, Yan J, Xiao W, Huang XW, Tang LC, Shi YQ, Song P, Gao JF. Stretchable, durable and asymmetrically wettable nanofiber composites with unidirectional water transportation capability for temperature sensing. *J Colloid Interface Sci.* **2023**;641:893.
35. Younes I, Rinaudo M. Chitin and chitosan preparation from marine. Sources structure properties and applications. *Mar Drugs.* **2015**;13:1133.
36. Guo P, Anderson JD, Bozell JJ, Zivanovic S. The effect of solvent composition on grafting gallic acid onto chitosan via carbodiimide. *Carbohydr Polym.* **2016**;140:171.
37. Li Q, Chen R, Cui TT, Bai YT, Hu J, Yu JF, Wang GF, Chen S. Robust gradient hydrogel-loaded nanofiber fleshy artificial skin via a coupled microfluidic electrospinning-reactive coating strategy. *Adv Healthcare Mater.* **2024**;13: 2304321.
38. Wu ZZ, Wang L, Bu NT, Chen XR, Duan J, Wu YX, Ma C, Pang J. All-natural and triple-inspired Janus electrospun fibers with integrated functions for high-performance liquid food packaging. *Chem Eng J.* **2024**;491: 151794.
39. Cai L, Zhu XY, Ruan HJ, Yang J, Wei W, Wu Y, Zhou LZ, Jiang HJ, Ji MH, Chen J. Curcumin-stabilized silver nanoparticles encapsulated in biocompatible electrospun nanofibrous scaffold for sustained eradication of drug-resistant bacteria. *J Hazard Mater.* **2023**;452: 131290.
40. Wei WL, Wang MY, Liu ZR, Zheng W, Tremblay PL, Zhang T. An antibacterial nanoclay- and chitosan-based quad composite with controlled drug release for infected skin wound healing. *Carbohydr Polym.* **2024**;324: 121507.
41. Li X, Zhang GW, Xu X, Zhao G, Liu YY, Yin SH. Fabrication of superhydrophobic surfaces on a glass substrate via hot embossing. *Ceram Int.* **2023**;49:26338.
42. Chen YX, Ao J, Zhang JT, Gao J, Hao LW, Jiang RJ, Zhang ZH, Liu ZN, Zhao J, Ren LQ. Bioinspired superhydrophobic surfaces, inhibiting or promoting microbial contamination? *Mater Today.* **2023**;67:468.
43. Lim H, Park Y, Jeong S, Kim H, Shin G, Choi K, Yang H. Highly durable, thermally stable, semi-transparent superhydrophobic surfaces for easy-cleaning of contaminants. *Prog Org Coat.* **2023**;179: 107537.
44. Li F, Su YJ, Pi GF, Ma P, Lei B. Biodegradable, biomimetic elastomeric, photoluminescent, and broad-spectrum antibacterial polycitrate-polypeptide-based membrane toward multifunctional biomedical implants. *ACS Biomater Sci Eng.* **2018**;4:3027.
45. Ren W, Huang X, Yan G, Yang J, Zhang G. Structuring multiscale porous architecture in polyether sulfone films for ultra-low dielectric constant. *Polymer.* **2023**;272: 125832.
46. Movaghgharnezhad S, Kim M, Min Lee S, Jeong H, Kim H, Gak Kim B, Kang P. Highly sensitive photodetector based on laser-generated graphene with 3D heterogeneous multiscale porous structures. *Mater Des.* **2023**;231: 112019.
47. Sun GC, Zhang JY, Li X, Hao BL, Xu FT, Liu KQ. Reuse of coal gangue to prepare adsorbent with multiscale pore structure for emulsified water removal. *Inorg Chem Commun.* **2023**;151: 110632.
48. Chen SW, Yang FC, Guo ZG. Transport and collection of water droplets interacting with bioinspired fibers. *Adv Colloid Interface Sci.* **2022**;309: 102779.

49. Menon S, Gurunadhan M. Droplet behavior in overexpanded supersonic two-phase jets. *Int J Multiphase Flow*. **2022**;152: 104076.
50. Hu X, Zhang Y, Yang J, Xiao K, Guo JH, Zhang XS. Magnetic digital microfluidic manipulation with mobile surface energy traps capable of releasable droplet dispensing. *Sensor Actua B-Chem*. **2023**;393: 134283.
51. Peng ZC, Liu RP, Xu ZG, Chi HJ, Wang Z, Zhao Y. Directional sweat transport window based on hydrophobic/hydrophilic Janus fabric enables continuous transfer and monitoring of sweat. *Appl Mater Today*. **2022**;29: 101623.
52. Feng WQ, Ueda E, Levkin P. Droplet microarrays: from surface patterning to high-throughput applications. *Adv Mater*. **2018**;30:1706111.
53. Sosa F, Carmickle A, Oliveira L, Sagheer M, Saleem M, Yu F, Altman M, Dikmen S, Denicol A, Sonstegard T, Larson C, Hansen P. Effects of the bovine SLICK1 mutation in PRLR on sweat gland area, FOXA1 abundance, and global gene expression in skin. *J Dairy Sci*. **2022**;105:9206.
54. Sardesai AU, Greyling CF, Lin K, Kumar RM, Muthukumar S, Prasad S. A new paradigm in tracking the dynamics of glucose and cortisol: an observational study from human sweat enabled by a skin sensor. *Biosens Bioelectron*. **2023**;14: 100377.
55. Wei L, Lv ZH, He YX, Cheng L, Qiu Y, Huang XZ, Ding C, Wu HP, Liu AP. In-situ admittance sensing of sweat rate and chloride level in sweat using wearable skin-interfaced microfluidic patch. *Sensor Actua B-Chem*. **2023**;379: 133213.
56. Lu C, Polak L, Rocha A, Pasolli HA, Chen S, Sharma N, Blanpain C, Fuchs E. Identification of stem cell populations in sweat glands and ducts reveals roles in homeostasis and wound repair. *Cell*. **2012**;150:136.
57. Xi P, He XC, Fan C, Zhu QL, Li Z, Yang YM, Du X, Xu TL. Smart Janus fabrics for one-way sweat sampling and skin-friendly colorimetric detection. *Talanta*. **2023**;259: 124507.
58. Mo L, Ma XD, Fan LF, Xin J, Yu H. Weavable, large-scaled, rapid response, long-term stable electrochemical fabric sensor integrated into clothing for monitoring potassium ions in sweat. *Chem Eng J*. **2023**;454: 140473.
59. Xiao G, Ju J, Li M, Wu HJ, Jian YH, Sun W, Wang W, Li CM, Qiao Y, Lu ZS. Weavable yarn-shaped supercapacitor in sweat-activated self-charging power textile for wireless sweat biosensing. *Biosens Bioelectron*. **2023**;235: 115389.
60. Yüzer E, Doğan V, Kılıç V, Şen M. Smartphone embedded deep learning approach for highly accurate and automated colorimetric lactate analysis in sweat. *Sensor Actua B-Chem*. **2022**;371: 132489.
61. OseiLartey P, Li D, Li J, Qin W, Guo K, Ma J. Fluoropolymer-based hybrid superhydrophobic nanocomposite coating with anti-fouling and self-cleaning properties for efficient oil/water separation. *Colloid Surface A*. **2022**;650: 129504.
62. Bao Y, Chang JX, Zhang YX, Chen L. Robust superhydrophobic coating with hollow SiO₂/PAA-b-PS Janus microspheres for self-cleaning and oil-water separation. *Chem Eng J*. **2022**;446: 136959.
63. Liu X, Zhang XD, Chen Q, Pan YM, Liu CT, Shen CY. A simple superhydrophobic/superhydrophilic Janus-paper with enhanced biocompatibility by PDMS and candle soot coating for actuator. *Chem Eng J*. **2021**;406: 126532.
64. Li WL, Liu K, Zhang YX, Guo S, Li ZX, Tan SC. A facile strategy to prepare robust self-healable superhydrophobic fabrics with self-cleaning, anti-icing, UV resistance, and antibacterial properties. *Chem Eng J*. **2022**;446: 137195.
65. Peng J, Wu LY, Zhang H, Wang B, Si Y, Jin SW, Zhu H. Research progress on eco-friendly superhydrophobic materials in environment, energy and biology. *Chem Commun*. **2022**;58:11201.
66. Zheng S, Li WZ, Ren YY, Liu Z, Zou XY, Hu Y, Guo JN, Sun Z, Yan F. Moisture-wicking, breathable, and intrinsically antibacterial electronic skin based on dual-gradient poly(ionic liquid) nanofiber membranes. *Adv Mater*. **2021**;34:2106570.
67. Xue B, Qin M, Wu JH, Luo DJ, Jiang Q, Li Y, Cao Y, Wang W. Electroresponsive supramolecular graphene oxide hydrogels for active bacteria adsorption and removal. *ACS Appl Mater Interfaces*. **2016**;8:15120.
68. Fahimirad S, Fahimirad Z, Sillanpää M. Efficient removal of water bacteria and viruses using electrospun nanofibers. *Sci Total Environ*. **2021**;751: 141673.
69. Shi LX, Liu X, Wang WS, Jiang L, Wang ST. A self-pumping dressing for draining excessive biofluid around wounds. *Adv Mater*. **2018**;31:1804187.
70. Xu Z, Fan JL, Tian WG, Ji X, Cui YQ, Nan QY, Sun FF, Zhang J. Cellulose-based pH-responsive janus dressing with unidirectional moisture drainage for exudate management and diabetic wounds healing. *Adv Funct Mater*. **2024**;34:2307449.
71. Zhou LB, Xu P, Dong PX, Ou XL, Du X, Chen Y, Zhang X, Guo WL, Gao GH. A self-pumping dressing with in situ modification of non-woven fabric for promoting diabetic wound healing. *Chem Eng J*. **2023**;457: 141108.
72. Tang L, Dang Y, Wang Y, Zhang YL, Hu TS, Ding CC, Wu H, Ni YH, Chen LH, Huang LL, Zhang M. Rapid fabrication of bionic pyrogallol-based self-adhesive hydrogel with mechanically tunable, self-healing, antibacterial, wound healing, and hemostatic properties. *Mat Sci Eng C-Mater*. **2022**;136: 212765.
73. Chen R, Zhao C, Chen ZP, Shi X, Zhu HX, Bu Q, Wang L, Wang CF, He H. A bionic cellulose nanofiber-based nanocage wound dressing for NIR-triggered multiple synergistic therapy of tumors and infected wounds. *Biomaterials*. **2022**;281: 121330.
74. Chen MS, Jin Y, Han X, Wang N, Deng XY, Liu HP. MSCs on an acellular dermal matrix (ADM) sourced from neonatal mouse skin regulate collagen reconstruction of granulation tissue during adult cutaneous wound healing. *RSC Adv*. **2017**;7:22998.
75. Zhao XW, Liu R, Tang TT, Liu Z, Liu XZ, Yu K, Zhang Y, Wang H. Promotion and monitor wound healing by anthocyanin enhanced light curing ϵ -poly-L-lysine hydrogel encapsulated Cu-MOF. *Chem Eng J*. **2024**;494: 152875.

Springer Nature or its licensor (e.g. a society or other partner) holds exclusive rights to this article under a publishing agreement with the author(s) or other rightsholder(s); author self-archiving of the accepted manuscript version of this article is solely governed by the terms of such publishing agreement and applicable law.